



**HAL**  
open science

## Continental configuration controls ocean oxygenation during the Phanerozoic

Alexandre Pohl, Andy Ridgwell, Richard G. Stockey, Christophe Thomazo, Andrew Keane, Emmanuelle Vennin, Christopher R. Scotese

► **To cite this version:**

Alexandre Pohl, Andy Ridgwell, Richard G. Stockey, Christophe Thomazo, Andrew Keane, et al.. Continental configuration controls ocean oxygenation during the Phanerozoic. *Nature*, 2022, 608 (7923), pp.523-527. 10.1038/s41586-022-05018-z . hal-03753039

**HAL Id: hal-03753039**

**<https://hal.science/hal-03753039v1>**

Submitted on 3 Dec 2024

**HAL** is a multi-disciplinary open access archive for the deposit and dissemination of scientific research documents, whether they are published or not. The documents may come from teaching and research institutions in France or abroad, or from public or private research centers.

L'archive ouverte pluridisciplinaire **HAL**, est destinée au dépôt et à la diffusion de documents scientifiques de niveau recherche, publiés ou non, émanant des établissements d'enseignement et de recherche français ou étrangers, des laboratoires publics ou privés.

1 Continental configuration controls ocean oxygenation  
2 during the Phanerozoic  
3

4 **Alexandre POHL<sup>1,2\*,\*\*</sup>, Andy RIDGWELL<sup>1\*</sup>, Richard G. STOCKEY<sup>3</sup>, Christophe**  
5 **THOMAZO<sup>2,4</sup>, Andrew KEANE<sup>5</sup>, Emmanuelle VENNIN<sup>2</sup>, Christopher R. SCOTESE<sup>6</sup>**

6 *<sup>1</sup>Department of Earth and Planetary Sciences, University of California, Riverside, CA,*  
7 *USA*

8 *<sup>2</sup>Biogéosciences, UMR 6282, UBFC/CNRS, Université Bourgogne Franche-Comté, 6*  
9 *boulevard Gabriel, F-21000 Dijon, France*

10 *<sup>3</sup>Department of Geological Sciences, Stanford University, Stanford, CA 94305, USA*

11 *<sup>4</sup>Institut Universitaire de France, Paris, France*

12 *<sup>5</sup>School of Mathematical Sciences and Environmental Research Institute, University*  
13 *College Cork, Cork, Ireland*

14 *<sup>6</sup>Department of Earth and Planetary Sciences, Northwestern University, Evanston,*  
15 *Illinois 60208, USA*

16  
17 *\*These authors contributed equally to this work*

18 *\*\*Corresponding author: [alexandre.pohl@u-bourgogne.fr](mailto:alexandre.pohl@u-bourgogne.fr)*

19  
20  
21  
22  
23  
24

25 **ABSTRACT**

26 **The early evolutionary and much of the extinction history of marine animals, is thought**  
27 **to be driven by changes in dissolved oxygen concentrations ( $[O_2]$ ) in the ocean<sup>1-3</sup>. In turn,**  
28  **$[O_2]$  is widely assumed to be dominated by the geological history of atmospheric oxygen**  
29 **( $pO_2$ )<sup>4,5</sup>. Here, in contrast, we show via a series of Earth system model experiments how**  
30 **continental rearrangement during the Phanerozoic drives profound variations in ocean**  
31 **oxygenation and induces a fundamental decoupling in time between upper-ocean and**  
32 **benthic  $[O_2]$ . We further identify the presence of state transitions in the global ocean**  
33 **circulation, which lead to extensive deep-ocean anoxia developing in the early**  
34 **Phanerozoic even under modern  $pO_2$ . The occurrence of stable kyr-scale oscillations in**  
35 **ocean oxygenation that we find also provides a causal mechanism that might explain**  
36 **elevated rates of metazoan radiation and extinction during the early Paleozoic<sup>6</sup>. The**  
37 **absence, in our modelling, of any simple correlation between global climate and ocean**  
38 **ventilation, and the occurrence of profound variations in ocean oxygenation independent**  
39 **of atmospheric  $pO_2$ , presents a challenge to the interpretation of marine redox proxies,**  
40 **but also points to a hitherto unrecognized role for continental configuration in the**  
41 **evolution of the biosphere.**

42

43 **MAIN TEXT**

44 The availability of dissolved oxygen in the ocean exerts a critical control on habitability for  
45 marine animals<sup>1,7</sup> and is thought to have dramatically impacted their evolution from the late  
46 Neoproterozoic and through the Phanerozoic Eon (541-0 Ma)<sup>1-3</sup>. Indeed, the emergence of the  
47 first unambiguous metazoans during the Ediacaran period (635–541 Ma) may have been  
48 triggered by the occurrence of ambient  $[O_2]$  sufficient to support the metabolism of a large  
49 body size<sup>1</sup>. Further increases in ocean oxygenation may have contributed to the Great

50 Ordovician Biodiversification Event<sup>8</sup> as well as the rise of large predatory fish in the  
51 Devonian<sup>9</sup>. Conversely, episodic deoxygenation is considered the primary kill mechanism  
52 during many of the major Phanerozoic mass extinction events, including the Late Ordovician<sup>10</sup>,  
53 Late Devonian<sup>11</sup> and end Permian<sup>7</sup>.

54 The past few decades have seen the development and application of a variety of  
55 geochemical redox proxies such as  $\delta^{238}\text{U}$ <sup>12</sup>,  $\delta^{98}\text{Mo}$ <sup>9</sup>, I/Ca<sup>13</sup> and iron speciation<sup>14</sup>, which have  
56 provided us with unprecedented insights into the Phanerozoic history of ocean oxygenation<sup>5,13</sup>.  
57 In parallel, numerical models have been instrumental in helping interpret the proxy trends and  
58 test hypotheses for the underlying driving mechanisms<sup>4,15</sup>. Principal amongst the ideas that  
59 have arisen is that changes in atmospheric  $p\text{O}_2$  can be inferred from the ocean<sup>4,5,15</sup>. However,  
60 for computational reasons, this link between ocean  $[\text{O}_2]$  and atmospheric  $p\text{O}_2$  has invariably  
61 been made without considering how ocean circulation may have changed through time<sup>4,5,15</sup>.  
62 While the importance of continental configuration for ocean circulation and surface climate  
63 has started to be studied systematically<sup>16–18</sup>, spatial patterns of ocean geochemistry and redox  
64 have only been considered in a limited number of continental configurations (e.g. refs<sup>7,19</sup>) and  
65 often analyzed in temporal isolation. Here we explicitly address this gap, employing an Earth  
66 System Model of intermediate complexity to quantify how continental configuration can  
67 modulate the distribution of  $[\text{O}_2]$  in the ocean, thereby leading us to a radically different  
68 conclusion regarding the inferences that can be drawn from marine redox proxy records.

69 We base our analysis on a series of past ocean circulation scenarios generated using  
70 cGENIE<sup>20</sup>, an Earth System Model of intermediate complexity designed to simulate the  
71 large-scale biogeochemical cycles and patterns in the ocean, and one that has previously been  
72 shown to be capable of simulating regional-scale distributions of  $[\text{O}_2]$  in the present-day  
73 ocean<sup>20</sup> as well as in the geological past<sup>19,21</sup> (see Methods, Extended Data Fig. 1). In these  
74 experiments, we consider both the potential role of changing ecological structure in the ocean

75 (using the size-structured plankton model of ref<sup>22</sup>) as well as the influence of temperature on  
76 metabolic rates (following ref<sup>23</sup>) in creating 3D realizations of the potential distribution of  
77 [O<sub>2</sub>] in the ocean. Based on the continental reconstructions of Scotese and Wright<sup>24</sup>, we  
78 conducted one simulation every 20 Myrs through the Phanerozoic, for a total of 28 simulated  
79 time slices. In order to help isolate the impact of continental configuration from other  
80 changes occurring through the Phanerozoic, only the continental configuration<sup>24</sup> (plus  
81 physical atmospheric boundary conditions – see Methods) was varied from one time slice to  
82 the other. Solar luminosity (1368 W m<sup>-2</sup>), atmospheric oxygen concentration (20.95 %), and  
83 ocean nutrient inventory (2.1 μmol kg<sup>-1</sup> PO<sub>4</sub>) were kept identical in every model run, and in a  
84 first series of simulations (#1), we also kept atmospheric *p*CO<sub>2</sub> fixed (at 2240 ppm, see  
85 Methods). We hence are not aiming to reconstruct the Phanerozoic evolution of climate here  
86 (see e.g. refs<sup>16,18</sup>), nor necessarily provide a reconstruction of past [O<sub>2</sub>] in the ocean or even  
87 recover modern distributions with high fidelity, but rather, expose the specific impact of  
88 changes in continental configuration on gross ocean oxygenation.

89         Despite assuming both invariant solar constant and *p*CO<sub>2</sub>, substantive variability in  
90 climate through the Phanerozoic occurs in the model (Fig. 1b). This is an expected result of  
91 sea-level driven changes in the proportion of absorptive ocean surface vs. more reflective  
92 land surface<sup>17,25</sup> as well as of continental latitudinal distribution, and in a principal  
93 component analysis conducted across all 28 time slices we find a strong positive correlation  
94 between global mean sea-surface temperature (SST) and global ocean surface area (Fig. 1e;  
95  $R^2 = 0.585$ ). Given our assumption of invariant *p*O<sub>2</sub> (deliberately chosen to expose the role of  
96 the continental configuration), we find a relatively straightforward and expected inverse  
97 relationship between mean ocean surface [O<sub>2</sub>] and SST (Fig. 1b, e) – driven primarily via  
98 changes in oxygen solubility and modulated by the latitudinal distribution of ocean surface  
99 area. Global mean subsurface (ca. 90–190 m depth in the model) [O<sub>2</sub>] exhibits a more

100 exaggerated temporal evolution (Fig. 1c). Respiration of organic matter exported from the  
101 ocean surface now strongly amplifies subsurface oxygen variability (Fig. 1c, e) and  
102 introduces new features unconnected to SST changes, such as the  $\sim 35 \mu\text{mol kg}^{-1}$  decrease  
103 from 460 to 400 Ma. This is our first hint of the importance of changing continental  
104 distribution and hence large-scale pattern of ocean circulation, which in the case of  
105 subsurface  $[\text{O}_2]$  is via changes in the resupply of nutrients to the surface. Even without  
106 attempting to simulate a realistic sequence of Phanerozoic climate states (and hence changing  
107 ocean surface oxygen solubility), our modelling provides hints as to the timing of Oceanic  
108 Anoxic Events (OAEs) during the Phanerozoic (Fig. 2, Extended Data Fig. 2). For instance,  
109 seafloor ocean deoxygenation develops in the paleo-Tethys during the Permian-Triassic  
110 transition (ca. 260 Ma)<sup>26</sup> and in the central Atlantic during the Early Cretaceous (ca. 120  
111 Ma)<sup>27</sup> and Late Cretaceous (ca. 100 Ma)<sup>28</sup>. That the Late Devonian OAE (380 Ma)<sup>29</sup> and  
112 Toarcian OAE (ca. 180 Ma)<sup>30</sup> are not captured by our simulations may be a result of the  
113 coarse model grid (for the Tethys Ocean during the Toarcian OAE in particular<sup>30</sup>; Fig. 2,  
114 Extended Data Fig. 2). This could also be interpreted as reflecting the need for a strong  
115 perturbation (warming and nutrient-driven increase in primary productivity) at that time to  
116 trigger an OAE, since the continental configuration itself is not particularly prone to ocean  
117 deoxygenation in our model simulations.

118 Our unexpected discovery from the numerical modelling is how variable global deep-  
119 ocean  $[\text{O}_2]$  (calculated as the mean of all benthic grid points in the model below 1000 m  
120 depth) is (Fig. 1d); ranging from  $30 \mu\text{mol kg}^{-1}$  (and near fully anoxic) to  $178 \mu\text{mol kg}^{-1}$  (a  
121 little higher than modern). The early Paleozoic (541 to 460 Ma) in particular stands out, and  
122 is characterized by anomalously poor deep seafloor oxygenation (generally  $< 45 \mu\text{mol kg}^{-1}$ )  
123 in the model, with an abrupt rise to  $171 \mu\text{mol kg}^{-1}$  at 440 Ma and thereafter mostly remaining  
124 above  $100 \mu\text{mol kg}^{-1}$  (Fig. 1d). The step change in benthic oxygenation simulated between

125 460 Ma and 440 Ma is similarly observed using an alternative set of continental  
126 reconstructions<sup>31</sup> (Extended Data Fig. 4). Simulated water age (the mean time since a water  
127 parcel was last exposed to the atmosphere) anti-correlates with mean global and benthic [O<sub>2</sub>]  
128 (Fig. 1d, e), while SST and global water age do not correlate (Fig. 1e; R<sup>2</sup> = 0.001), pointing  
129 to the dominance of a paleogeographical control on deep-ocean oxygenation.

130 To further simplify the attribution of causes of benthic [O<sub>2</sub>] variability through the  
131 Phanerozoic and eliminate global climate change and resulting solubility-driven upper-ocean  
132 [O<sub>2</sub>] variations as explanatory factors, we carried out a second series of model experiments  
133 (#2) in which we kept mean global SST and surface oxygenation largely invariant (Fig. 3).  
134 Climate detrending was achieved by varying *p*CO<sub>2</sub> in the model. Variance in mean benthic  
135 [O<sub>2</sub>] (Fig. 3d) is now if anything, even greater than in #1 (Fig. 1d) and the general trend of a  
136 poorly oxygenated early Paleozoic deep ocean still stands. These results confirm that benthic  
137 anoxia in the early Paleozoic ocean results from changes in the deep-ocean circulation in the  
138 model, rather than temperature-driven variations in upper-ocean [O<sub>2</sub>]. Sensitivity tests  
139 demonstrate that global mean temporal trends and spatial oxygenation patterns are largely  
140 independent of whether a temperature-dependent (Fig. 1) or fixed remineralization profile  
141 (Extended Data Fig. 5) is assumed. Similarly, patterns of benthic [O<sub>2</sub>] are only weakly  
142 impacted by uncertainties in the position of mid-ocean ridges (Extended Data Figs. 6, 7).

143 The role of continental configuration in creating conditions of extreme deep-ocean  
144 deoxygenation and weakened ventilation (old water mass ages) during the early Paleozoic  
145 (prior to 440 Ma in series #1 (Fig. 1d), and prior to 420 Ma in series #2 (Fig. 3d)), arises from  
146 the existence of state transitions in the large-scale circulation of the ocean in the model.  
147 Using series #1 as an example, the oldest time slices (540 – 500 Ma) are characterized by a  
148 poorly ventilated seafloor with deep waters forming over the South Pole (Figs. 1d and 2,  
149 Extended Data Fig. 8a). At 480 and 460 Ma, the ocean circulation oscillates between the

150 previous poorly-ventilated state and a better-ventilated state, the latter state subsequently  
151 becoming stabilized at 440 Ma by further tectonic rearrangement (Figs. 1d and 2, Extended  
152 Data Fig. 8a). Of course, the differences in the two simulation series illustrate that the climate  
153 state also influences the ocean circulation regimes (contrast Figs. 1 and 3; see also Extended  
154 Data Figs. 8 and 9). Several lines of evidence suggest that these state transitions are a robust  
155 characteristic of the early Paleozoic, at least in the cGENIE model. Indeed, additional  
156 simulations conducted using idealized land-sea masks reveal that these state transitions may  
157 be a characteristic feature of continental configurations with one pole free of land (Extended  
158 Data Fig. 10; Methods), such as the one of the early Paleozoic (Fig. 2), and a similar  
159 reorganization of the global ocean circulation has previously been shown to best explain the  
160 expansion of seafloor anoxia during Late Ordovician glaciation (Extended Data Fig. 10 and  
161 ref.<sup>21</sup>).

162         The occurrence of climate-driven state transitions in ocean circulation and oxygenation  
163 is well established in the context of changes in Atlantic and Pacific basin meridional  
164 overturning since the last glacial maximum (21 ka)<sup>32,33</sup>. In contrast, the potential for ocean  
165 state transitions in deeper time has received much less attention but is no less important (e.g.  
166 ref.<sup>21</sup>). We also have good reason to conclude that the occurrence of oscillatory ocean  
167 circulation modes is not an artifact of the particular model used here and may occur as a  
168 transitional regime between different stable steady-states (Extended Data Fig. 10). For  
169 instance, oscillations have previously been identified in both (ocean-only) 3D ocean  
170 circulation models<sup>34,35</sup> and 3D ocean circulation models coupled to simplified representations  
171 of atmospheric dynamics (Earth System Models of intermediate complexity)<sup>36,37</sup>. Non-steady  
172 solutions in volume-integrated ocean temperature are also hinted at in a number of recent  
173 fully coupled GCM simulations under specific continental configurations and climate  
174 states<sup>16</sup>. Further work conducted using higher-resolution Earth system models, e.g. of the



175 Coupled Model Intercomparison Project phase 6 generation, will be important to distinguish  
176 robust from model-dependent modes of ocean circulation, although identifying the boundary  
177 conditions giving rise to oscillatory modes will be computationally challenging.

178 Our finding of a fundamental decoupling of subsurface and benthic [O<sub>2</sub>] during the  
179 Phanerozoic (Fig. 1e; R<sup>2</sup> = 0.001) implies that no simple relationship exists during the  
180 Phanerozoic amongst the concentrations of oxygen in the atmosphere, the subsurface ocean,  
181 and at the seafloor. Furthermore, the highly non-linear and chaotic nature of the system  
182 means that even very minor changes in continental configuration (e.g. contrast 460 vs. 440  
183 Ma, Figure 2) can induce dramatic re-organizations of large-scale circulation and hence  
184 ocean oxygenation, and similarly, confusticate any predictable relationship between changes  
185 in atmospheric *p*CO<sub>2</sub> (and climate) and ocean oxygenation. This has implications not only for  
186 how we interpret deep-ocean redox proxy records and specifically proxies for the global areal  
187 extent of seafloor anoxia<sup>5</sup> (e.g., δ<sup>238</sup>U<sup>12</sup>, δ<sup>98</sup>Mo<sup>9</sup>), but also how we understand the underlying  
188 controls on ocean anoxia and infer changes in atmospheric composition. For instance, Stolper  
189 and Keller<sup>38</sup> analyzed the ratio of Fe<sup>3+</sup> to total Fe (Fe<sup>3+</sup>/ΣFe) in hydrothermally altered basalts  
190 formed in ocean basins to quantitatively reconstruct deep-ocean [O<sub>2</sub>] over the last 3500  
191 Myrs. Their results suggest that the deep ocean became oxygenated only in the Phanerozoic  
192 and probably not until the late Paleozoic (<420 Myr). Our simulations support the vision of a  
193 poorly oxygenated early Paleozoic ocean<sup>4,5,38</sup> (until ca. 440 Ma in the model, see Figs. 1d,  
194 3d). However, while Fe<sup>3+</sup>/ΣFe data is interpreted as reflecting a rise in atmospheric oxygen  
195 concentrations<sup>38</sup>, our Earth System simulations in contrast suggest that deep-ocean  
196 oxygenation around 440–420 Ma could have been a consequence of continental  
197 rearrangement and concomitant changes in ocean circulation and ventilation. The implication  
198 is that early Phanerozoic atmospheric *p*O<sub>2</sub> need not have been appreciably lower than  
199 modern, which aligns with the measurements of atmospheric oxygen trapped in fluid-gas

200 inclusions of halite<sup>39</sup>. Furthermore, the step changes in early Paleozoic seafloor oxygenation  
201 are indicative of bistability between deep-ocean circulation states; that is, for certain  
202 continental configurations multiple advection and convection patterns will co-exist (what is  
203 observed depends on the initial conditions of the simulation). Switches between such states  
204 could provide an explanation to the swings<sup>5</sup> in early Paleozoic global anoxia extent  
205 documented on grounds of  $\delta^{238}\text{U}^{40-42}$  and  $\delta^{98}\text{Mo}^{41,43}$ . Uncertainties in both the model and  
206 geological data preclude us from determining if our simulated scenario may have actually  
207 taken place in the geological past, and we recognize that continental rearrangement is also  
208 not exclusive of secular variation in other drivers of ocean anoxia, such as atmospheric  
209 oxygen, ocean nutrient inventory, and global warming<sup>13,19,21,26</sup>. That said, and despite our  
210 idealized boundary conditions and invariant atmospheric chemistry, there are shared temporal  
211 trends (albeit with different timings and interval durations) with recent I/Ca-based oxygen  
212 proxy compilations<sup>13</sup>, namely: low oxygenation in the early and late Paleozoic with a high  
213 during the Devonian, and peak values occurring prior to late Cenozoic cooling.

214 Finally, our results have implications for the evolution of marine animal ecosystems  
215 through the Phanerozoic. If kyr-scale oscillations in ocean oxygenation were a characteristic  
216 feature of early Paleozoic oceans, as supported by the high-resolution Mo record of ref.<sup>44</sup> and  
217 our modelling (Extended Data Fig. 8), this would lend support to arguments linking the  
218 progressive (here: paleogeographical) stabilization of a steady-state Earth system to  
219 decreasing extinction rates through the Phanerozoic<sup>6,45</sup>.

220

## 221 MAIN TEXT REFERENCES

- 222 1. Payne, J. L. *et al.* Two-phase increase in the maximum size of life over 3.5 billion  
223 years reflects biological innovation and environmental opportunity. *Proc. Natl. Acad.*  
224 *Sci. U. S. A.* **106**, 24–27 (2009).

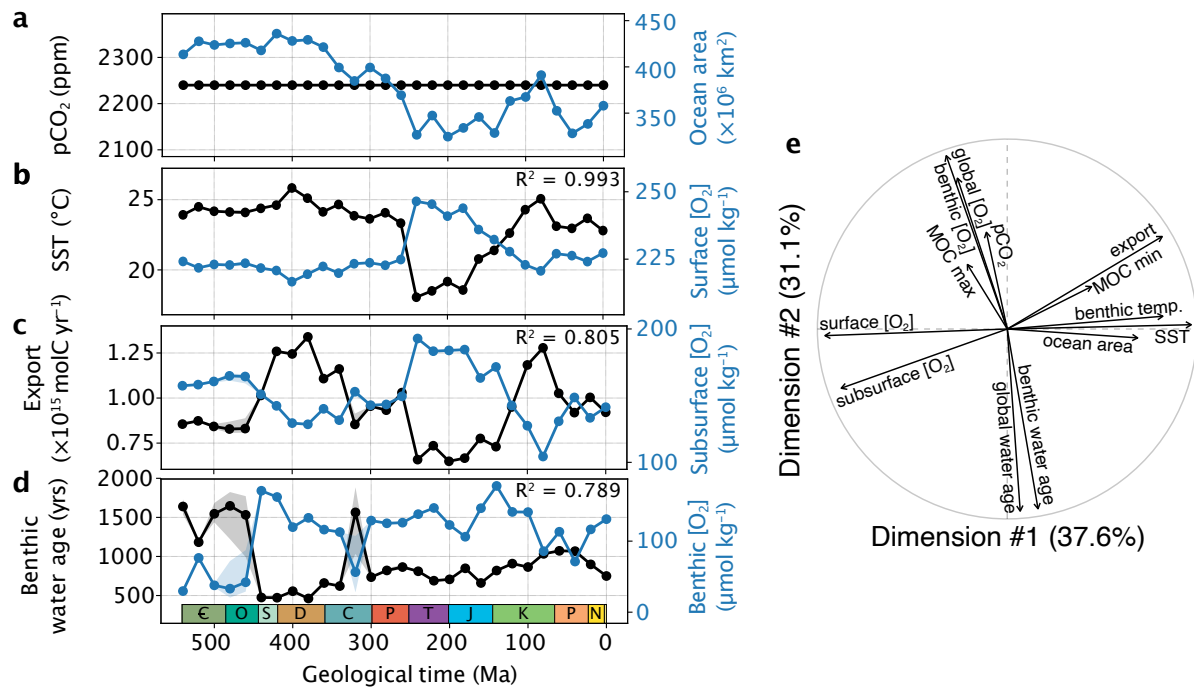
- 225 2. Cole, D. B. *et al.* On the co-evolution of surface oxygen levels and animals.  
226 *Geobiology* **18**, 260–281 (2020).
- 227 3. Sperling, E. A., Knoll, A. H. & Girguis, P. R. The Ecological Physiology of Earth’s  
228 Second Oxygen Revolution. *Annu. Rev. Ecol. Evol. Syst.* **46**, 215–235 (2015).
- 229 4. Krause, A. J. *et al.* Stepwise oxygenation of the Paleozoic atmosphere. *Nat. Commun.*  
230 **9**, 4081 (2018).
- 231 5. Tostevin, R. & Mills, B. J. Reconciling proxy records and models of Earth’s  
232 oxygenation during the Neoproterozoic and Palaeozoic. *Interface Focus* **10**, 20190137  
233 (2020).
- 234 6. Kocsis, Á. T., Reddin, C. J., Alroy, J. & Kiessling, W. The r package divDyn for  
235 quantifying diversity dynamics using fossil sampling data. *Methods Ecol. Evol.* **10**,  
236 735–743 (2019).
- 237 7. Penn, J. L., Deutsch, C., Payne, J. L. & Sperling, E. A. Temperature-dependent  
238 hypoxia explains biogeography and severity of end-Permian marine mass extinction.  
239 *Science* **362**, eaat1327 (2018).
- 240 8. Edwards, C. T., Saltzman, M. R., Royer, D. L. & Fike, D. A. Oxygenation as a driver  
241 of the Great Ordovician Biodiversification Event. *Nat. Geosci.* **10**, 925–929 (2017).
- 242 9. Dahl, T. W., Hammarlund, E. U. & Anbar, A. D. Devonian rise in atmospheric oxygen  
243 correlated to the radiations of terrestrial plants and large predatory fish. *Proc. Natl.*  
244 *Acad. Sci.* **107**, 17911–17915 (2010).
- 245 10. Zou, C. *et al.* Ocean euxinia and climate change “double whammy” drove the Late  
246 Ordovician mass extinction. *Geology* **46**, 535–538 (2018).
- 247 11. Bond, D., Wignall, P. B. & Racki, G. Extent and duration of marine anoxia during the  
248 Frasnian-Famennian (Late Devonian) mass extinction in Poland, Germany, Austria  
249 and France. *Geol. Mag.* **141**, 173–193 (2004).

- 250 12. Lau, K. V. *et al.* Marine anoxia and delayed Earth system recovery after the end-  
251 Permian extinction. *Proc. Natl. Acad. Sci.* **113**, 2360–2365 (2016).
- 252 13. Lu, W. *et al.* Late inception of a resiliently oxygenated upper ocean. *Science* **5**,  
253 eaar5372 (2018).
- 254 14. Sperling, E. A. *et al.* A long-term record of early to mid-Paleozoic marine redox  
255 change. *Sci. Adv.* (2021) doi:10.1126/sciadv.abf4382.
- 256 15. Lenton, T. M. *et al.* Earliest land plants created modern levels of atmospheric oxygen.  
257 *Proc. Natl. Acad. Sci. U. S. A.* 201604787 (2016).
- 258 16. Valdes, P., Scotese, C. & Lunt, D. Deep Ocean Temperatures through Time. *Clim.*  
259 *Past* **17**, 1483–1506 (2021).
- 260 17. Farnsworth, A. *et al.* Climate Sensitivity on Geological Timescales Controlled by  
261 Nonlinear Feedbacks and Ocean Circulation. *Geophys. Res. Lett.* **6**, 19 (2019).
- 262 18. Scotese, C. R., Song, H., Mills, B. J. W. & van der Meer, D. G. Phanerozoic  
263 paleotemperatures: The earth’s changing climate during the last 540 million years.  
264 *Earth-Science Rev.* 103503 (2021) doi:10.1016/j.earscirev.2021.103503.
- 265 19. Monteiro, F. M., Pancost, R. D., Ridgwell, A. & Donnadieu, Y. Nutrients as the  
266 dominant control on the spread of anoxia and euxinia across the Cenomanian-Turonian  
267 oceanic anoxic event (OAE2): Model-data comparison. *Paleoceanography* **27**, (2012).
- 268 20. Ridgwell, A. *et al.* Marine geochemical data assimilation in an efficient Earth system  
269 model of global biogeochemical cycling. *Biogeosciences* **4**, 87–104 (2007).
- 270 21. Pohl, A. *et al.* Vertical decoupling in Late Ordovician anoxia due to reorganization of  
271 ocean circulation. *Nat. Geosci.* **14**, (2021).
- 272 22. Ward, B. A. *et al.* EcoGENIE 0.1: plankton ecology in the cGENIE Earth system  
273 model. *Geosci. Model Dev.* **11**, 4241–5267 (2018).
- 274 23. Crichton, K. A., Wilson, J. D., Ridgwell, A. & Pearson, P. N. Calibration of key

- 275 temperature-dependent ocean microbial processes in the cGENIE. muffin Earth system  
276 model. *Geophys. Model Dev. Discuss.* (2020).
- 277 24. Scotese, C. R. & Wright, N. PALEOMAP Paleodigital Elevation Models  
278 (PaleoDEMS) for the Phanerozoic (PALEOMAP Project, 2018).  
279 <https://www.earthbyte.org/paleodem-resource-scotese-and-wright-2018/> (2018).
- 280 25. Pohl, A. *et al.* Quantifying the paleogeographic driver of Cretaceous carbonate  
281 platform development using paleoecological niche modeling. *Palaeogeogr.*  
282 *Palaeoclimatol. Palaeoecol.* **514**, 222–232 (2019).
- 283 26. Hülse, D. *et al.* End-Permian marine extinction due to temperature-driven nutrient  
284 recycling and euxinia. *Nat. Geosci.* **14**, (2021).
- 285 27. Baudin, F. & Riquier, L. The late hauterivian faraoni ‘oceanic anoxic event’: An  
286 update. *Bull. la Soc. Geol. Fr.* **185**, 359–377 (2014).
- 287 28. Laugié, M. *et al.* Exploring the impact of Cenomanian paleogeography and marine  
288 gateways on oceanic oxygen. *Paleoceanogr. Paleoclimatology* **36**, e2020PA004202  
289 (2021).
- 290 29. De Vleeschouwer, D. *et al.* Timing and pacing of the Late Devonian mass extinction  
291 event regulated by eccentricity and obliquity. *Nat. Commun.* **8**, 2268 (2017).
- 292 30. Ruvalcaba Baroni, I. *et al.* Ocean Circulation in the Toarcian (Early Jurassic): A Key  
293 Control on Deoxygenation and Carbon Burial on the European Shelf. *Paleoceanogr.*  
294 *Paleoclimatology* **33**, 994–1012 (2018).
- 295 31. Torsvik, T. H. BugPlates : Linking Biogeography and Palaeogeography Software  
296 Installation. (2009).
- 297 32. Ferreira, D., Marshall, J., Ito, T. & McGee, D. Linking Glacial-Interglacial States to  
298 Multiple Equilibria of Climate. *Geophys. Res. Lett.* **45**, 9160–9170 (2018).
- 299 33. Jaccard, S. L. & Galbraith, E. D. Large climate-driven changes of oceanic oxygen

- 300 concentrations during the last deglaciation. *Nat. Geosci.* **5**, 151–156 (2012).
- 301 34. Weijer, W. & Dijkstra, H. A. Multiple oscillatory modes of the global ocean  
302 circulation. *J. Phys. Oceanogr.* **33**, 2197–2213 (2003).
- 303 35. Sirkes, Z. & Tziperman, E. Identifying a damped oscillatory thermohaline mode in a  
304 general circulation model using an adjoint model. *J. Phys. Oceanogr.* **31**, 2297–2306  
305 (2001).
- 306 36. Meissner, K. J., Eby, M., Weaver, A. J. & Saenko, O. A. CO<sub>2</sub> threshold for millennial-  
307 scale oscillations in the climate system: Implications for global warming scenarios.  
308 *Clim. Dyn.* **30**, 161–174 (2008).
- 309 37. Haarsma, R. J., Opsteegh, J. D., Selten, F. M. & Wang, X. Rapid transitions and ultra-  
310 low frequency behaviour in a 40 kyr integration with a coupled climate model of  
311 intermediate complexity. *Clim. Dyn.* **17**, 559–570 (2001).
- 312 38. Stolper, D. A. & Keller, C. B. A record of deep-ocean dissolved O<sub>2</sub> from the oxidation  
313 state of iron in submarine basalts. *Nature* **553**, 323–327 (2018).
- 314 39. Brand, U. *et al.* Atmospheric oxygen of the Paleozoic. *Earth-Science Rev.* **216**, (2021).
- 315 40. Dahl, T. W. *et al.* Reorganisation of earth's biogeochemical cycles briefly oxygenated  
316 the oceans 520 myr ago. *Geochemical Perspect. Lett.* **10**, 210–220 (2019).
- 317 41. Wei, G. Y. *et al.* Global marine redox evolution from the late Neoproterozoic to the  
318 early Paleozoic constrained by the integration of Mo and U isotope records. *Earth-  
319 Science Rev.* **214**, 103506 (2021).
- 320 42. Wei, G. Y. *et al.* Marine redox fluctuation as a potential trigger for the Cambrian  
321 explosion. *Geology* **46**, 587–590 (2018).
- 322 43. Kendall, B. *et al.* Uranium and molybdenum isotope evidence for an episode of  
323 widespread ocean oxygenation during the late ediacaran period. *Geochim. Cosmochim.  
324 Acta* **156**, 173–193 (2015).

- 325 44. Dahl, T. W. *et al.* Brief oxygenation events in locally anoxic oceans during the  
326 Cambrian solves the animal breathing paradox. *Sci. Rep.* **9**, 1–9 (2019).
- 327 45. Payne, J. L., Bachan, A., Heim, N. A., Hull, P. M. & Knope, M. L. The evolution of  
328 complex life and the stabilization of the Earth system: Complex life and the Earth  
329 system. *Interface Focus* **10**, (2020).
- 330



331

332 Figure 1. Earth System Model results for simulations at 2240 ppm CO<sub>2</sub> (series #1). (a)

333 Atmospheric pCO<sub>2</sub> and global ocean area. (b) Globally averaged sea-surface temperatures and

334 globally averaged ocean-surface oxygen concentrations. (c) Total export production and

335 globally averaged subsurface (ca. 90–190 m depth) oxygen concentrations. (d) Globally

336 averaged benthic water age and benthic oxygen concentrations, both extracted below 1000 m

337 depth. (e) Principal component analysis (Methods). In panels b–d, the linear correlation

338 coefficient (R<sup>2</sup>) value is provided in the upper-right corner. For each variable and age, the mean

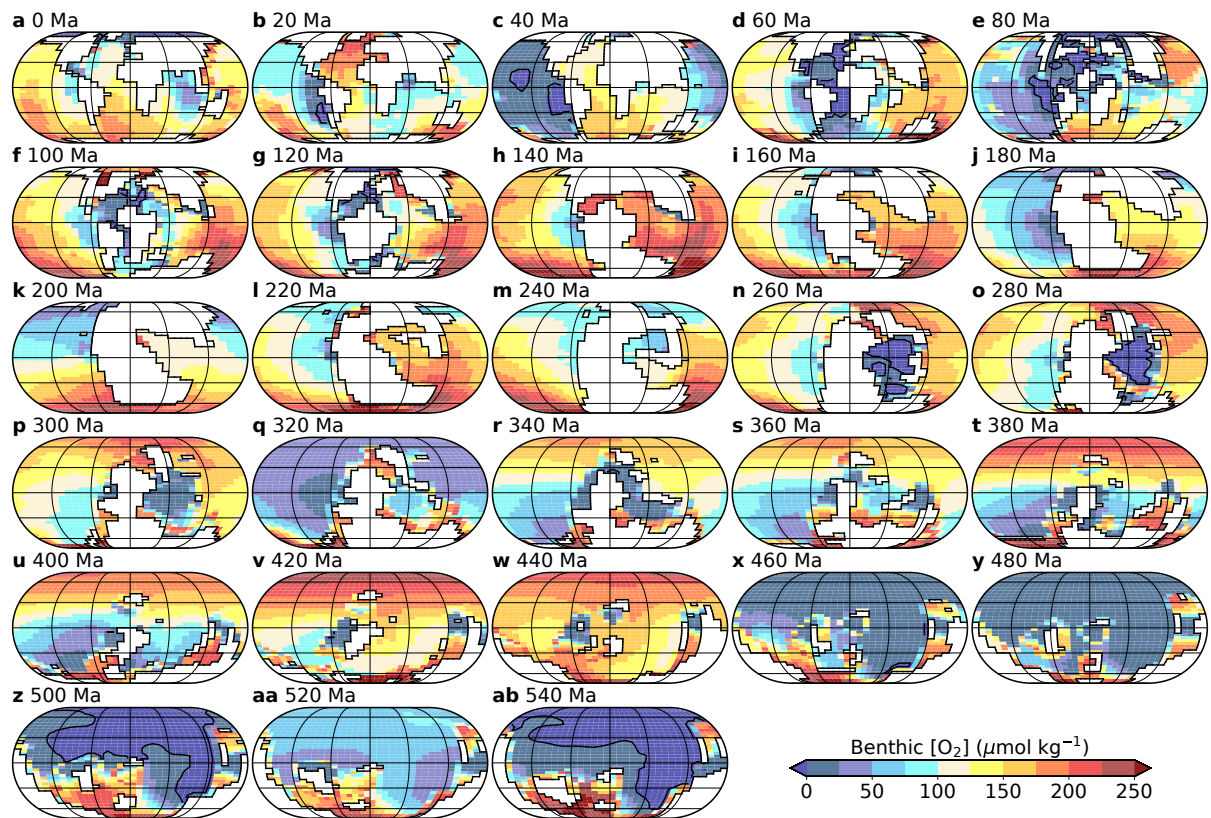
339 value simulated over the last 5000 years of the model run is shown (point), while envelopes

340 (shading) represent the range of values simulated over the same time interval (for simulations

341 exhibiting oscillations). MOC: meridional overturning circulation.

342

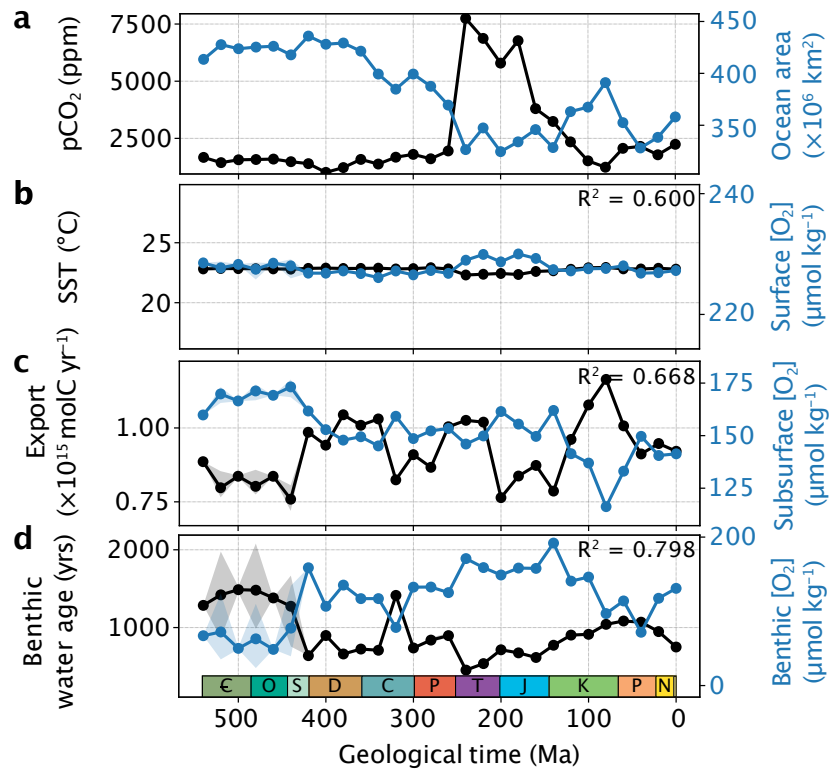




343

344 Figure 2. Benthic oxygen concentrations for simulations at 2240 ppm CO<sub>2</sub> (series #1). Eckert  
 345 IV projection. Emerged continental masses are shaded white. Results are averaged over the last  
 346 5000 years. See Extended Data Fig. 2 for magnified versions of 7 panels with redox proxy data  
 347 points and Extended Data Fig. 3 for the meridional overturning circulation and regions of deep-  
 348 water formation.

349



350

351 Figure 3. Earth System Model results for simulations in which we varied  $p\text{CO}_2$  in order to  
 352 approximately ‘correct’ for the paleogeographical impacts on climate (series #2). Panels (a-d)  
 353 and panel description as per for Fig. 1. Note that in this series of experiments, surface  
 354 oxygenation and mean global SST (b) are largely invariant.

355

## 356 **METHODS**

### 357 **Description of the model**

358 cGENIE<sup>20</sup> – an ‘Earth System Model of intermediate complexity’ – is based around a 3-  
359 dimensional ocean circulation model which, for speed, is coupled to a 2D energy-moisture-  
360 balance atmospheric component. We configured the model on a 36×36 equal-area grid with  
361 16 unevenly spaced vertical levels to a maximum 5500 m depth in the ocean. The cycling of  
362 carbon and associated tracers in the ocean is based on a single (phosphate) nutrient limitation  
363 of biological productivity accounting for plankton ecology based on Ward et al.<sup>22</sup> and Wilson  
364 et al.<sup>46</sup>, but adopts the Arrhenius-type temperature-dependent scheme for the remineralization  
365 of organic matter exported to the ocean interior of Crichton et al.<sup>23</sup>. We further modify the  
366 ecological model of Ward et al.<sup>22</sup> to account for limitation of productivity under sea ice, re-  
367 scale the global mean annual C/P ratio of exported particulate organic matter to match that of  
368 the standard model (106)<sup>47</sup>, and only diagnose the ocean surface mixed layer depth for  
369 calculating light attenuation rather than entrain this into the physical circulation. We include  
370 a sulphate (SO<sub>4</sub><sup>2-</sup>) tracer as an electron acceptor in the model in addition to dissolved oxygen,  
371 such that when O<sub>2</sub> starts to approach zero, sulphate reduction occurs in association with the  
372 remineralization of organic matter. The hydrogen sulphide (H<sub>2</sub>S) thereby created is  
373 transported via ocean circulation and oxidized in the presence of O<sub>2</sub> to re-form sulphate. Note  
374 that we do not include a nitrogen cycle (and hence nitrate reduction), nor methanogenesis in  
375 our model tracer configuration. See ref.<sup>48</sup> and ref.<sup>49</sup> for details of the overall ocean redox  
376 scheme.

377 Despite its low spatial resolution, cGENIE satisfactorily simulates first-order ocean [O<sub>2</sub>]  
378 spatial patterns and values for the present-day ocean when configured with pre-industrial  
379 boundary conditions such as 278 ppm CO<sub>2</sub> (Extended Data Fig. 1 and ref.<sup>20</sup>), as well as in the  
380 geological past<sup>19,21</sup>. For instance, simulations for Oceanic Anoxic Event 2 conducted using

381 cGENIE (ref.<sup>19</sup>, their Fig. 2f,g) compare well with simulations conducted using the more  
382 complex model IPSL-CM5A2 (ref.<sup>28</sup>, their Fig. 10), in terms of both global extent of anoxia  
383 and response to gateway alteration.

#### 384 **Description of the numerical experiments**

385 We adopted the (flat-bottomed) Phanerozoic continental reconstructions of Scotese and  
386 Wright<sup>24</sup>, but substituted the deep-ocean bathymetry of Müller et al.<sup>50</sup> when available (140  
387 Ma – 0 Ma) in order to account for mid-ocean ridges. In order to specifically quantify the  
388 impact of paleogeographical evolution, we kept solar luminosity ( $1368 \text{ W m}^{-2}$ ), atmospheric  
389 oxygen concentrations (20.95 %), and ocean nutrient inventory ( $2.1 \mu\text{mol kg}^{-1} \text{ PO}_4$ ),  
390 invariant. We employed a null eccentricity-minimum obliquity orbital configuration, which  
391 provides an equal mean annual insolation to both hemispheres with minimum seasonal  
392 contrasts. Atmospheric  $\text{CO}_2$  concentration was kept fixed in series #1 (2240 ppm) but varied  
393 in series #2 in order to approximately ‘correct’ for the paleogeographical impacts on climate.  
394 These forcing combinations ensured that simulated ocean temperatures are in the right order  
395 of magnitude compared with the Phanerozoic proxy-derived trend<sup>18</sup>. The mean Phanerozoic  
396 tropical ( $25^\circ\text{S}$ – $25^\circ\text{N}$ ) sea-surface temperature is  $29.67^\circ\text{C}$  (standard deviation:  $1.88^\circ\text{C}$ ) in  
397 series #1 (mean of  $29.39^\circ\text{C}$  and standard deviation of  $0.45^\circ\text{C}$  in series #2) compared to a  
398 mean of  $28.1^\circ\text{C}$  (standard deviation:  $2.51^\circ\text{C}$ ) in the data compilation<sup>18</sup>.

399 To generate the physical atmospheric boundary conditions required by cGENIE for each  
400 different continental configuration, we ran FOAM<sup>51</sup> general circulation model experiments  
401 for 2 to 3 kyrs, until deep-ocean temperature equilibrium. We then derived the 2D wind  
402 speed and wind stress, and 1D zonally-averaged albedo forcing fields required by the  
403 cGENIE model, using the ‘muffingen’ open-source software (DOI:  
404 [10.5281/zenodo.5500687](https://doi.org/10.5281/zenodo.5500687)), following the methods employed in ref<sup>52</sup>.

405 Simulations were initialized with a sea-ice free ocean and homogeneous temperature and  
406 salinity in the ocean (5 °C and 33.9 ‰, respectively) and integrated for a total of 20,000  
407 years. Data is presented reflecting either the average over the last 5,000 years of the  
408 simulation (e.g., Fig. 2), or the mean and range of any oscillation over the last 5,000 years  
409 (e.g., Figs 1, 3), as detailed in the figure captions.

#### 410 **Principal component analysis**

411 Principal components analyses (PCA) of Fig. 1 and Extended Data Fig. 5 were performed  
412 using, for each variable, the mean value simulated over the last 5000 years of the model  
413 simulations. For each variable, a total of 28 values was thus obtained (one value for each of  
414 the 28 time slices, from 540 Ma to 0 Ma every 20 Myrs). We considered 13 variables: surface  
415 [O<sub>2</sub>], subsurface [O<sub>2</sub>], benthic [O<sub>2</sub>], global [O<sub>2</sub>], global water age, benthic water age, sea-  
416 surface temperature ('SST'), benthic temperature, pCO<sub>2</sub>, meridional overturning circulation  
417 maximum ('MOC max') and minimum ('MOC min'), export production ('export'; i.e., the  
418 flux of organic carbon produced in the ocean photic zone by primary producers that is not  
419 recycled (remineralised) before sinking deeper in the water column) and total ocean area. The  
420 PCA was conducted using the 'PCA' function of the R package 'FactoMineR'<sup>53</sup> and the first  
421 two axes / principal components were represented (capturing ca. 68 % of the variance in both  
422 cases). The objective here is not to provide a thorough PCA analysis but rather to (1) confirm  
423 the robustness of the correlations illustrated in the form of time-series and R<sup>2</sup> in the other  
424 panels of Fig. 1 and Extended Data Fig. 5 and (2) provide information on the correlation (or  
425 not) of additional key variables in a synthetic and graphical manner.

#### 426 **Additional discussion on ocean circulation regimes**

427 Most of the simulations in Extended Data Figs. 8a and 8b show that ocean dynamics obtain  
428 stable steady-state solutions. However, amongst these are cases where the system overshoots  
429 (for example, compare 0 Ma and 120 Ma in Extended Data Fig. 8a) before approaching a

430 steady-state solution. This may imply the presence of an unstable oscillatory mode, in  
431 agreement with the linear stability analysis of low-resolution GCM steady states under  
432 present-day conditions<sup>34,35</sup>. The simulations in Extended Data Fig. 8 reveal that, depending  
433 on changes to continental configuration, the steady-state solutions can lose stability, resulting  
434 in stable oscillations. It is known that, under certain climate conditions, advective feedbacks  
435 in the ocean circulation can destabilize the steady state<sup>54</sup>. Simulations for 540 Ma and 500  
436 Ma in Extended Data Figs.8a and 8b, respectively, are cases of steady-state solutions with  
437 oscillatory modes that are linearly stable, but only weakly stable, resulting in clear examples  
438 of damped oscillations. Since the frequencies of the damped and self-sustained oscillations  
439 (500 and 520 Ma in Extended Data Fig. 8b, respectively) are very similar, the transition could  
440 represent a Hopf bifurcation, resulting in self-sustained oscillations (characterized by  
441 fluctuations in circulation pattern and strength) around an unstable steady state.

442 In order to better understand the model behavior and ultimately, the nature of the state  
443 transitions in the global ocean circulation, we conducted additional cGENIE simulations  
444 using two contrasting, idealized continental configurations featuring either a latitudinal strip  
445 of land from the North Pole to the Southern Hemisphere mid latitudes ('Drake world'<sup>55</sup>), or a  
446 strip of land extending from the North Pole to the South Pole ('ridge world'<sup>55</sup>) (Extended  
447 Data Fig. 10). Drake world, with a pole free of land (i.e., purely oceanic at all longitudes),  
448 schematically represents the continental configuration of the early Paleozoic (or a high  
449 latitude circumpolar path such as in the late Cenozoic), while ridge world represents an early  
450 Mesozoic-like continental arrangement with landmasses present from the North Pole to the  
451 South Pole (see Fig. 2).

452 With Drake world, at low pCO<sub>2</sub> levels, deep-water formation takes place at the North  
453 Pole, where a slightly higher hemispherical fraction of land cover with lower thermal inertia  
454 favors winter cooling over the surrounding ocean and convection (label #1 in Extended Data

455 Figs. 10a and 10b). As atmospheric CO<sub>2</sub> is steadily increased across a series of experiments,  
456 the onset of a first set of oscillations, between  $\times 5.5$  and  $\times 7.5$  CO<sub>2</sub> (label #2), marks the  
457 appearance of a new mode of ocean circulation that stabilizes in the subsequent stable steady  
458 state at around  $\times 8.25$  CO<sub>2</sub> (label #3). Then, a new set of oscillations, from  $\times 9$  to  $\times 9.75$  CO<sub>2</sub>,  
459 marks another step toward the weakening of the deep-water formation over the North Pole  
460 and strengthening over the South Pole (label #4). A third stable equilibrium finally stabilizes  
461 above  $\times 10.75$  CO<sub>2</sub> (label #5). Each set of oscillations thus marks the shift to a new regime of  
462 steady-state circulation and the ultimate result is a shift in the locus of deep-water formation  
463 from the North Pole (with lands barriers) to the South Pole (oceanic) in response to global  
464 warming from  $\times 4$  to  $\times 16$  CO<sub>2</sub>. A comparable (but latitudinally reversed) behavior was  
465 previously observed by Pohl et al.<sup>21</sup> for the latest Ordovician. In response to global warming  
466 (their Figs. 4e to 4i, see also Extended Data Fig. 10c), the locus of deep-water formation  
467 shifts in their simulations from the South Pole (with lands) to the North Pole (oceanic). This  
468 is very similar to the change in ocean circulation simulated between 460 Ma and 440 Ma in  
469 simulation series #1 (Fig. 2), although the state transition here involves continental  
470 rearrangement in addition to global warming (global sea-surface temperature increases from  
471 24.1°C at 460 Ma to 24.38°C at 440 Ma). No similar state transition is observed using the  
472 ridge world configuration (Extended Data Fig. 10a).

473

#### 474 **METHODS REFERENCES**

- 475 46. Wilson, J. D., Monteiro, F. M., Schmidt, D. N., Ward, B. A. & Ridgwell, A. Linking  
476 Marine Plankton Ecosystems and Climate: A New Modeling Approach to the Warm  
477 Early Eocene Climate. *Paleoceanogr. Paleoclimatology* **33**, 1439–1452 (2018).
- 478 47. Cao, L. *et al.* The role of ocean transport in the uptake of anthropogenic CO<sub>2</sub>.  
479 *Biogeosciences* **6**, 375–390 (2009).

- 480 48. T. Reinhard, C. *et al.* Oceanic and atmospheric methane cycling in the cGENIE Earth  
481 system model - Release v0.9.14. *Geosci. Model Dev.* **13**, 5687–5706 (2020).
- 482 49. Velde, S. J. Van De, Hülse, D., Reinhard, C. T. & Ridgwell, A. Iron and sulfur cycling  
483 in the cGENIE. muffin Earth system model (v0.9.21). *Geosci. Model Dev.* **14**, 2713–  
484 2745 (2021).
- 485 50. Müller, R. D., Sdrolias, M., Gaina, C., Steinberger, B. & Heine, C. Long-term sea-  
486 level fluctuations driven by ocean basin dynamics. *Science* **319**, 1357–1362 (2008).
- 487 51. Jacob, R. L. Low frequency variability in a simulated atmosphere-ocean system.  
488 (University of Wisconsin Madison, 1997).
- 489 52. Crichton, K., Ridgwell, A., Lunt, D., Farnsworth, A. & Pearson, P. Data-constrained  
490 assessment of ocean circulation changes since the middle Miocene in an Earth system  
491 model. *Clim. Past Discuss.* 1–36 (2020) doi:10.5194/cp-2019-151.
- 492 53. Lê, S., Josse, J. & Husson, F. FactoMineR: An R package for multivariate analysis. *J.*  
493 *Stat. Softw.* **25**, 1–18 (2008).
- 494 54. Weijer, W. *et al.* Stability of the Atlantic Meridional Overturning Circulation: A  
495 Review and Synthesis. *J. Geophys. Res. Ocean.* **124**, 5336–5375 (2019).
- 496 55. Ferreira, D., Marshall, J. & Campin, J. M. Localization of deep water formation: Role  
497 of atmospheric moisture transport and geometrical constraints on ocean circulation. *J.*  
498 *Clim.* **23**, 1456–1476 (2010).
- 499 56. Garcia, H. *et al.* *World Ocean Atlas 2018, Volume 3: Dissolved Oxygen, Apparent*  
500 *Oxygen Utilization, and Dissolved Oxygen Saturation.* (2019).
- 501 57. Marsh, R. *et al.* Bistability of the thermohaline circulation identified through  
502 comprehensive 2-parameter sweeps of an efficient climate model. *Clim. Dyn.* **23**, 761–  
503 777 (2004).
- 504 58. DeVries, T. & Holzer, M. Radiocarbon and Helium Isotope Constraints on Deep



505 Ocean Ventilation and Mantle-3He Sources. *J. Geophys. Res. Ocean.* **124**, 3036–3057  
506 (2019).

507 59. Song, H. *et al.* The onset of widespread marine red beds and the evolution of  
508 ferruginous oceans. *Nat. Commun.* **8**, (2017).

509 60. Melchin, M. J., Mitchell, C. E., Holmden, C. & Štorch, P. Environmental changes in  
510 the Late Ordovician-early Silurian: Review and new insights from black shales and  
511 nitrogen isotopes. *Geol. Soc. Am. Bull.* **125**, 1635–1670 (2013).

512 61. Pohl, A., Nardin, E., Vandenbroucke, T. R. A. & Donnadieu, Y. High dependence of  
513 Ordovician ocean surface circulation on atmospheric CO<sub>2</sub> levels. *Palaeogeogr.*  
514 *Palaeoclimatol. Palaeoecol.* **458**, 39–51 (2016).

515 62. Meyer, K. M., Ridgwell, A. & Payne, J. L. The influence of the biological pump on  
516 ocean chemistry: implications for long-term trends in marine redox chemistry, the  
517 global carbon cycle, and marine animal ecosystems. *Geobiology* **14**, 207–219 (2016).

518

## 519 **CODE AVAILABILITY**

520 The version of the cGENIE code used in this paper is tagged as release v0.9.29 and has a  
521 DOI: 10.5281/zenodo.5885685. Necessary boundary condition files are included as part of  
522 the code release. Configuration files for the specific experiments presented in the paper can  
523 be found in the installation subdirectory: `genie-`  
524 `userconfigs/MS/pohletal.Nature.2022`. Details of the experiments, plus the command  
525 line needed to run each one, are given in the `readme.txt` file in that directory. A manual  
526 describing code installation, basic model configuration, and an extensive series of tutorials is  
527 provided (DOI: 10.5281/zenodo.5500696). The FOAM output is hosted on Zenodo (DOI:  
528 10.5281/zenodo.5780096).

## 529 **ACKNOWLEDGMENTS**

530 The authors thank 4 anonymous reviewers for their comments, and J. Mossinger for editorial  
531 handling. This project has received funding from the European Union's Horizon 2020 research  
532 and innovation programme under the Marie Skłodowska-Curie grant agreement No. 838373.  
533 Calculations were partly performed using HPC resources from DNUM CCUB (Centre de  
534 Calcul de l'Université de Bourgogne). A.R. acknowledges support from NSF grants 1736771  
535 and EAR-2121165, as well as from the Heising-Simons Foundation. This is a contribution to  
536 UNESCO project IGCP 735 "Rocks and the Rise of Ordovician Life" (Rocks n' ROL).

#### 537 **AUTHOR CONTRIBUTIONS**

538 A.P. and A.R. designed the study and wrote the manuscript with input from all co-authors.  
539 AP. and A.R. conducted the FOAM and cGENIE experiments. A.P., A.R. and A.K. led the  
540 analysis of the model results. C.R.S. produced the continental reconstructions.

#### 541 **COMPETING INTERESTS**

542 The authors declare no competing interests.

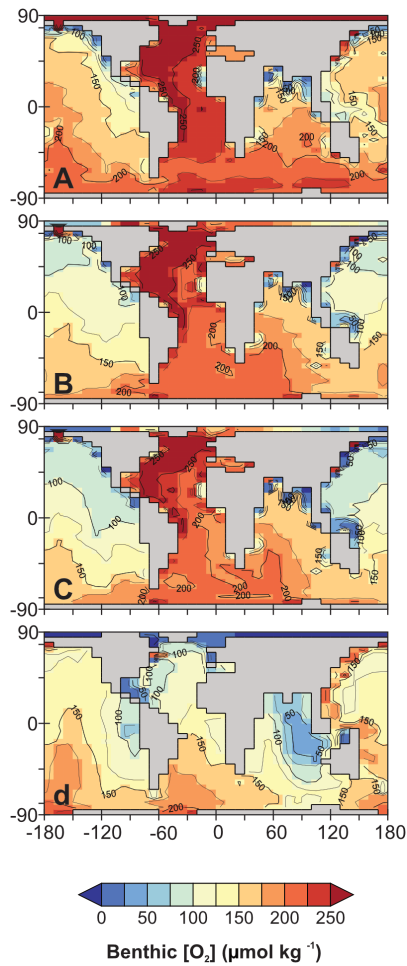
#### 543 **ADDITIONAL INFORMATION**

544 **Correspondence and requests for materials** should be addressed to A.P. and A.R.

545 **Peer review information.**

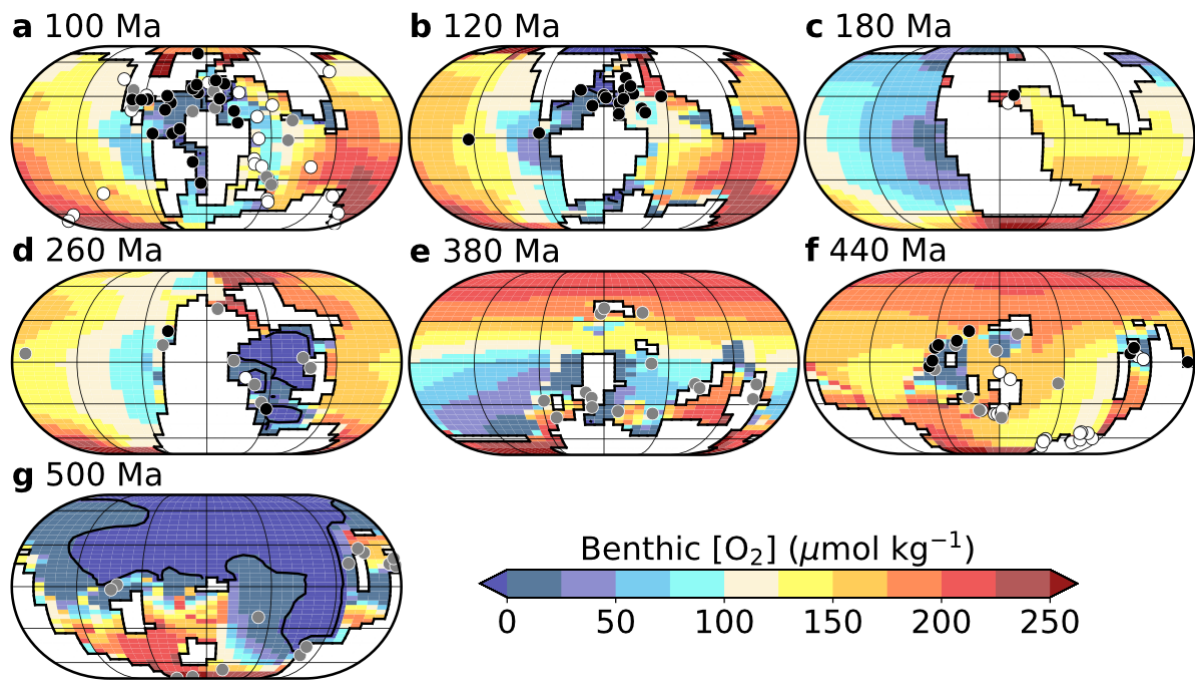
546 **Reprints and permissions information** is available at [www.nature.com/reprints](http://www.nature.com/reprints).

547



549 Extended Data Figure 1: Comparison of modern observations of seafloor [O<sub>2</sub>] with the  
 550 cGENIE model. Results are shown for different (modern) continental grids, boundary  
 551 conditions, and biogeochemical cycling parameterization assumptions. Projection is equal-  
 552 area rectangular, and the color-scale is chosen to approximately match that in Figure 2. (a)  
 553 Present-day distribution of [O<sub>2</sub>] globally at the seafloor, for which we re-grid the World  
 554 Ocean Atlas 2018<sup>56</sup> data to the modern continental grid of ref.<sup>47</sup> and show the oxygen  
 555 concentration in the deepest model grid point. Apparent is both the production and  
 556 southwards propagation (via North Atlantic Deep Water (NADW)) of highly oxygenated  
 557 waters from the North Atlantic, and oxygenated deep-water production and mixing around  
 558 Antarctica. (b) Benthic [O<sub>2</sub>] distribution for the ‘standard’ modern ocean circulation of ref.<sup>47</sup>  
 559 run at 278 ppm CO<sub>2</sub>, plus simplified biological export scheme. The large-scale patterns of  
 560 benthic [O<sub>2</sub>] are reasonably reproduced, with the exception of too weak mixing of oxygen

561 around the Southern Ocean, itself caused by a weak simulated Antarctic Circumpolar Current  
562 (ACC) and the difficulty in adequately representing the Drake Passage at this resolution. The  
563 slightly too-low compared to observations values in the North Pacific are an additional  
564 consequence of this. (c) Test of substituting the simplified biological export scheme of ref.<sup>47</sup>  
565 with the explicit ecosystem model used here in the Phanerozoic series of simulations (but still  
566 at 278 ppm CO<sub>2</sub>). The slightly greater export simulated by the ecological model reduces  
567 benthic [O<sub>2</sub>] by ca. 10-20 μmol kg<sup>-1</sup> while leaving the large-scale patterns largely unaltered.  
568 (d) Deep-sea oxygenation in the 0 Ma Phanerozoic simulation (as per Figure 2, panel a) run  
569 at 2240 ppm CO<sub>2</sub>. Without flux adjustment applied in the simplified cGENIE 2D EMBM  
570 atmosphere (see ref.<sup>57</sup>) there is virtually no NADW, explaining the relatively poor and South-  
571 to-North oxygenation of the Atlantic. The Indian Ocean is also too poorly oxygenated,  
572 although the general pattern in the Pacific is reproduced. There are several main reasons for  
573 this model-data mismatch. Firstly, directly re-gridding from a relatively coarse resolution  
574 GCM (FOAM) creates a highly restricted and shallow Drake Passage (Extended Data Figure  
575 7a, 0 Ma), precluding a strong ACC forming. More pertinently, the Phanerozoic simulation  
576 series (Figure 2) are all run at 2240 ppm. The resulting much-warmer-than-modern ocean is  
577 associated with the absence of any sea-ice formation and lower seawater oxygen solubility,  
578 likely explaining at least some of the spatial pattern and much of the lower global mean [O<sub>2</sub>]  
579 inventory (Extended Data Figure 8a, 0 Ma). In terms of ventilation and water mass idealized  
580 mean age (not shown), the Atlantic, lacking an AMOC is far too old, whereas the Indian and  
581 Pacific oceans are similar to the inverse modelling of ref.<sup>58</sup> despite the aforementioned issues  
582 with the Drake Passage and that the 0 Ma simulation is run at 2240 ppm CO<sub>2</sub>.



583

584 Extended Data Figure 2: Selected redox proxy data vs. the corresponding model oxygenation

585 realization. Benthic oxygen concentrations for simulations at 2240 ppm  $\text{CO}_2$  (series #1).

586 Eckert IV projection. Emerged continental masses are shaded white. Results are averaged

587 over the last 5000 years. Black (white) dots represent anoxic (oxic) conditions and grey

588 points represent possible or intermittent anoxia, for 100 Ma after ref.<sup>28</sup>, for 120 Ma after

589 ref.<sup>27</sup>, for 180 Ma after ref.<sup>30</sup>, for 260 Ma after ref.<sup>26</sup>, for 380 and 500 Ma after ref.<sup>59</sup>, and for

590 440 Ma after ref.<sup>60</sup>. These time slices have been chosen to represent regularly-spaced periods

591 during the Phanerozoic, typified by oceanic anoxic events. The last 100 Myrs are deliberately

592 left aside because (i) the ocean is overall well oxygenated during this time interval and (ii)

593 our constant boundary conditions (deliberately chosen to isolate the role of tectonics from

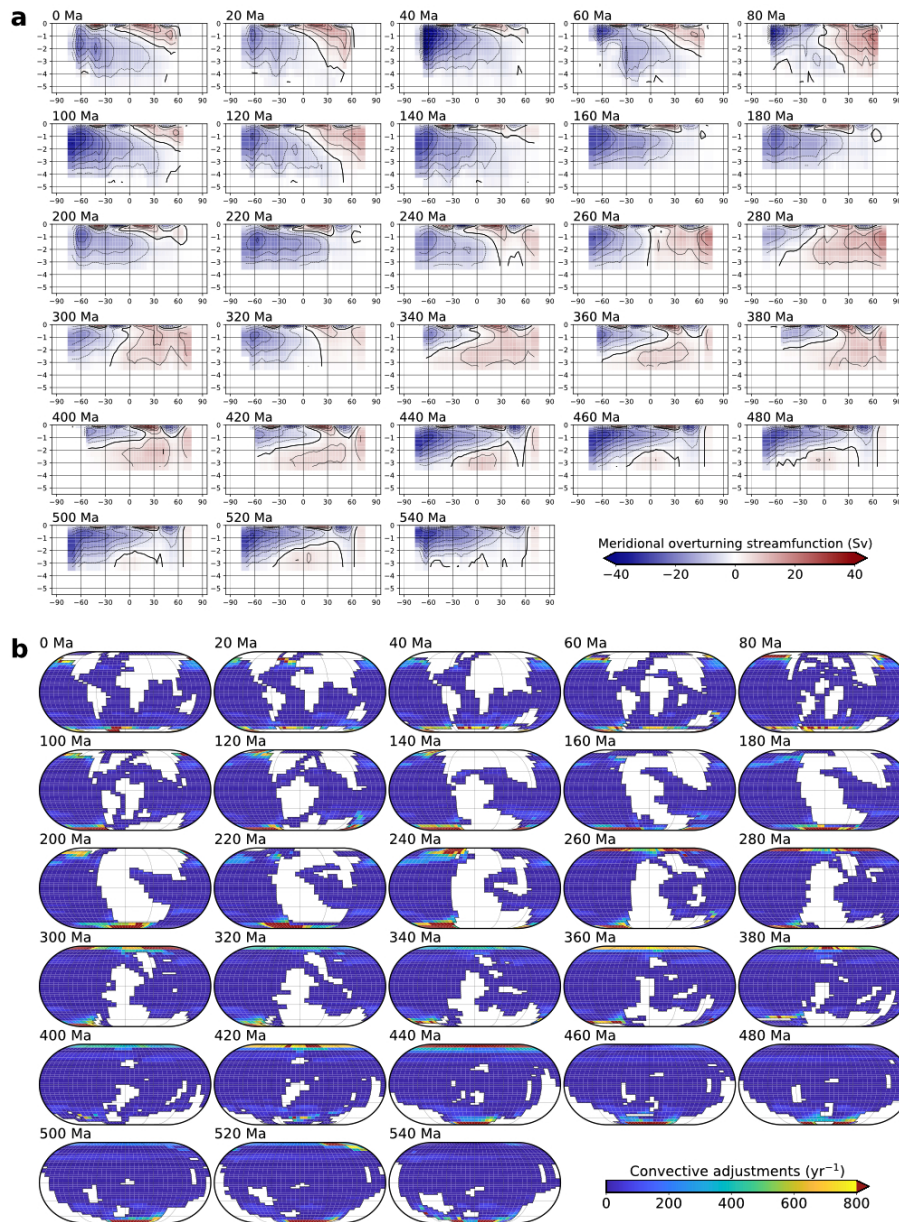
594 climate, see main text) do not (and indeed, do not intent to) reproduce the pronounced

595 cooling trend through the Cenozoic (especially from Early Eocene Climate Optimum (ca. 50

596 Ma) onwards), precluding direct model-data comparison.

597

598



599

600 Extended Data Figure 3: Deep-ocean circulation for simulations at 2240 ppm CO<sub>2</sub> (series #1).

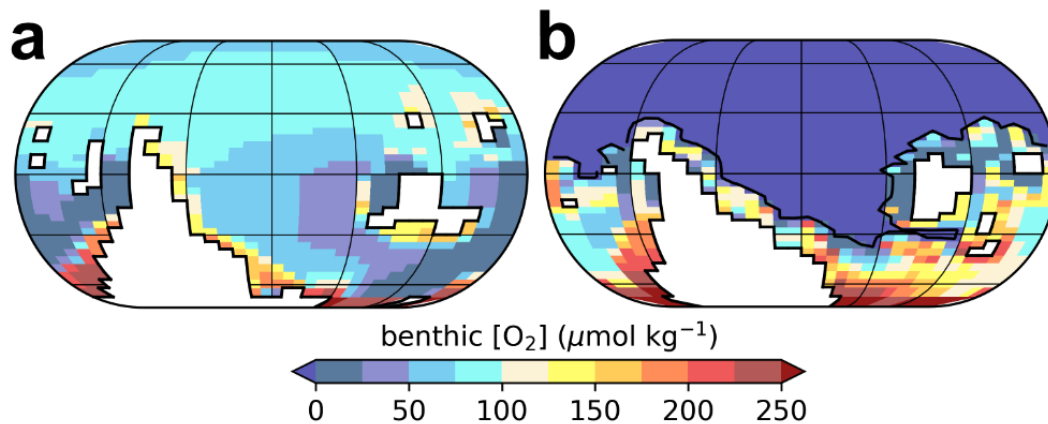
601 (a) Meridional overturning stream function, in Sv (sverdrup, 1 Sv = 10<sup>6</sup> m<sup>3</sup> s<sup>-1</sup>). A negative

602 (blue) stream function corresponds to an anticlockwise circulation. (b) Annual distribution of

603 convective adjustments across the water column. Emerged continental masses are shaded

604 white. Eckert IV projection. Results are averaged over the last 5000 years.

605



606

607 Extended Data Figure 4: Sensitivity of benthic [O<sub>2</sub>] to the continental reconstruction.

608 Benthic oxygen concentrations for simulations at 2240 ppm CO<sub>2</sub> (like series #1) at 440 Ma

609 (a) and 460 Ma (b), using the continental reconstructions of BugPlates<sup>31</sup>, with

610 topography/bathymetry after ref.<sup>61</sup>. Eckert IV projection. Emerged continental masses are

611 shaded white. Results are averaged over the last 5000 years. Panels (a) and (b) are identical to

612 panels (w) and (x) of Fig. 2 except that simulations have been conducted using another

613 continental reconstruction. Note that although we simulate sulphate reduction in cGENIE,

614 with SO<sub>4</sub><sup>2-</sup> being used as the electron acceptor for the remineralization of organic matter in

615 the ocean interior once dissolved O<sub>2</sub> has become depleted (see ref.<sup>48</sup>), small negative O<sub>2</sub>

616 concentrations can arise when multiple geochemical reactions compete simultaneously for

617 the same depleted oxygen pool. However, because the product of sulphate reduction –

618 hydrogen sulphide (H<sub>2</sub>S) – has fast oxidation kinetics in the presence of free oxygen, the

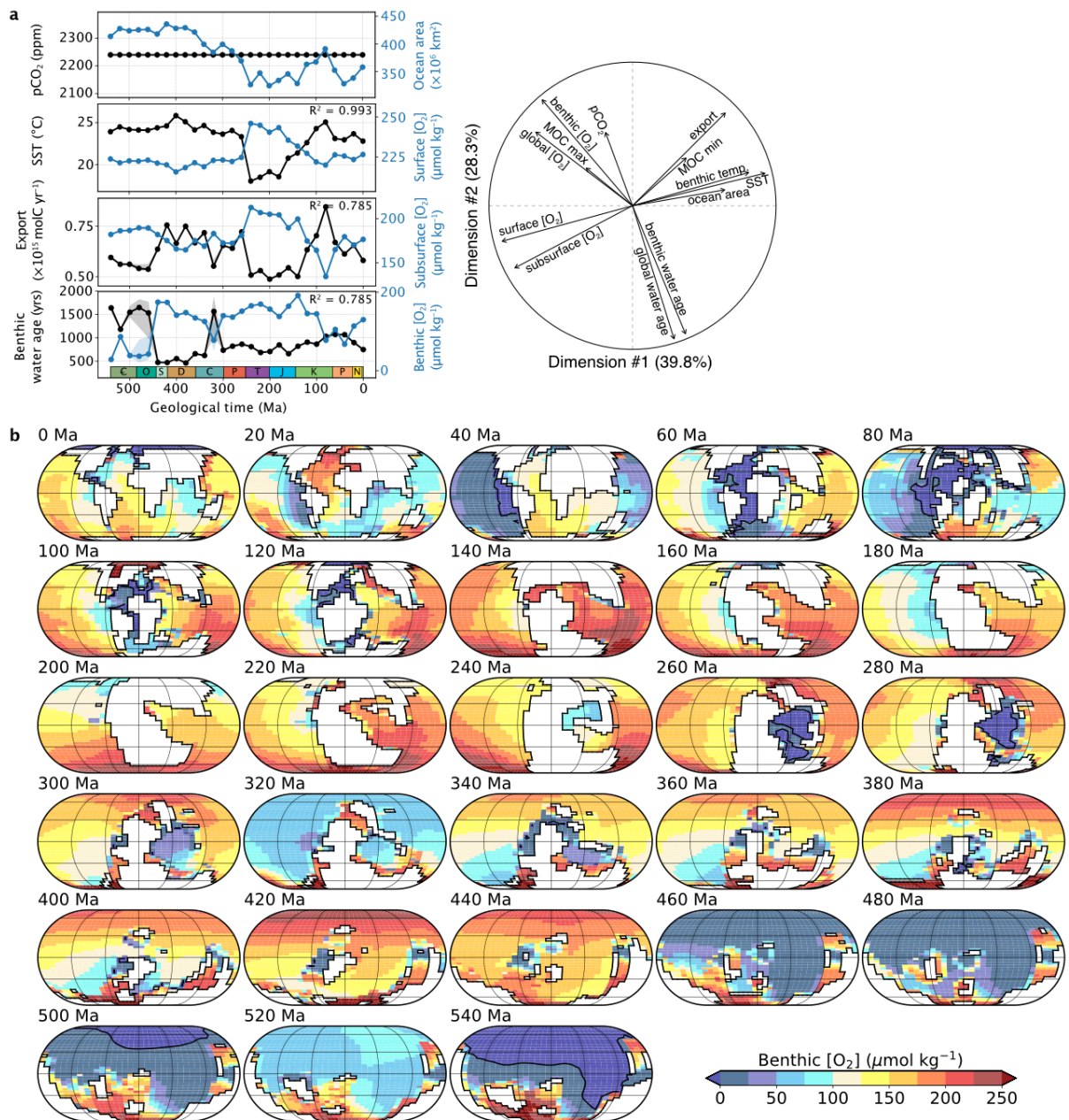
619 transport of H<sub>2</sub>S from anoxic to oxic areas closely mirrors the transport and fate of ‘negative

620 oxygen’ (see ref.<sup>62</sup>) and the overall redox landscape is largely independent of this small

621 modelled oxygen over-consumption.

622

623



624

625 Extended Data Fig. 5. Sensitivity to the remineralization scheme. Earth System Model results

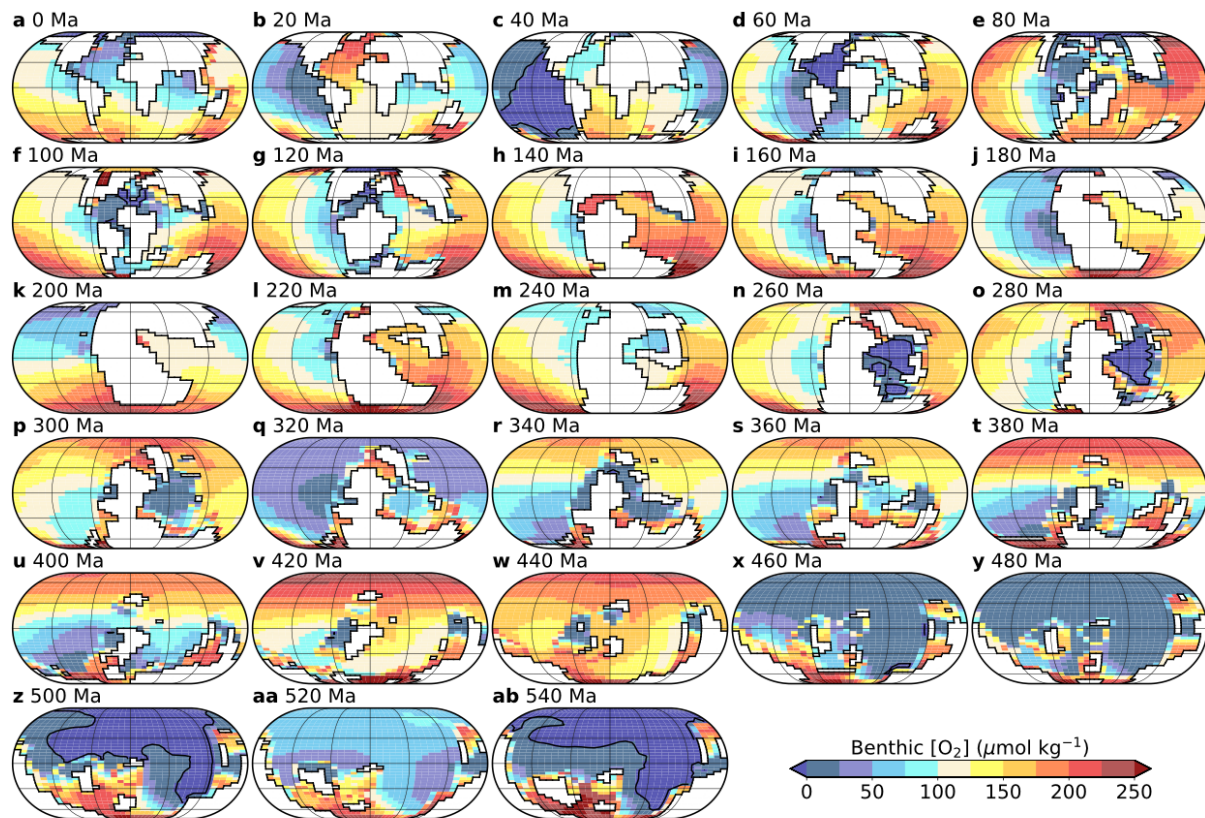
626 for simulations at 2240 ppm CO<sub>2</sub> (like #1) but with no dependence of remineralization on

627 temperature. (a) Same as Fig. 1. (b) Same as Fig. 2.

628

629

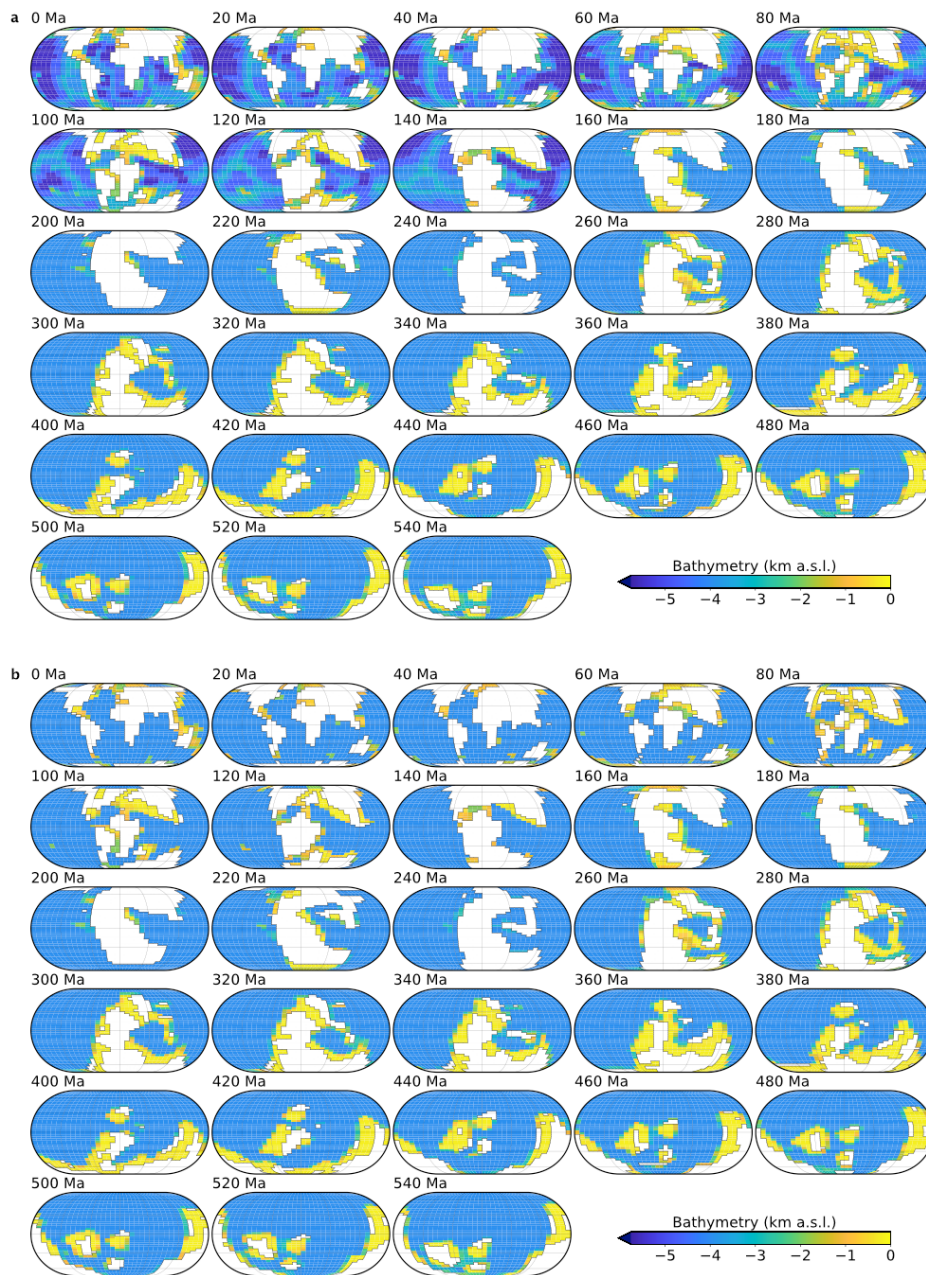




630

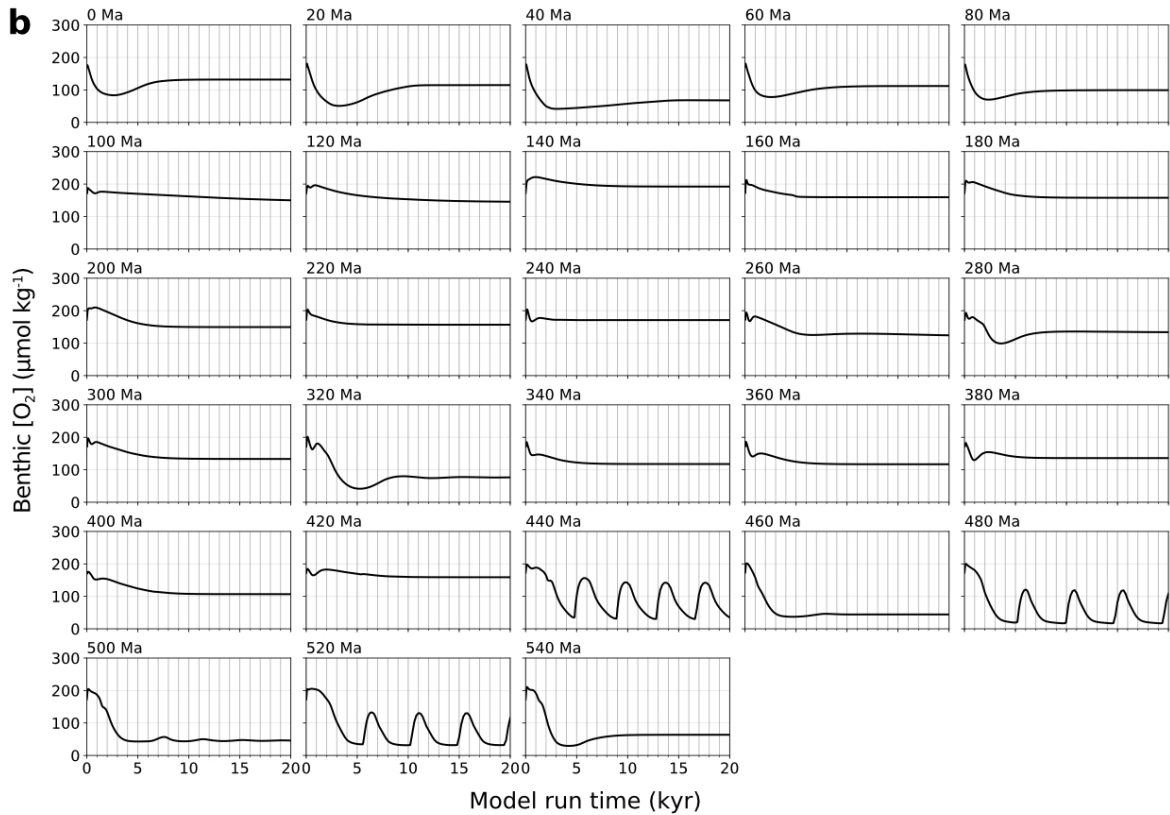
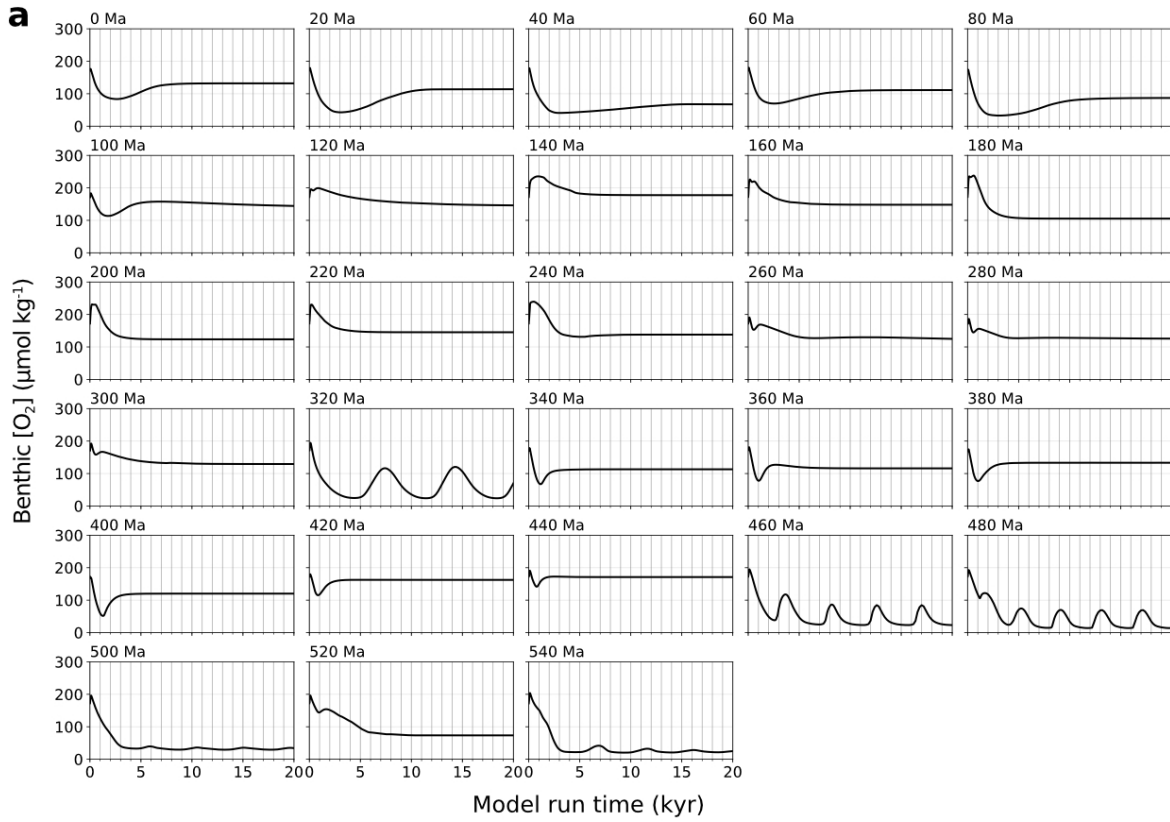
631 Extended Data Figure 6. Sensitivity of benthic  $[\text{O}_2]$  to deep-ocean bathymetry. Benthic  
 632 oxygen concentrations for simulations at 2240 ppm  $\text{CO}_2$  (like #1) but with no mid-ocean  
 633 ridges (see Extended Data Fig. 7). Results are averaged over the last 5000 years. Emerged  
 634 continental masses are shaded white. Eckert IV projection.

635



636

637 Extended Data Fig. 7: Bathymetric reconstructions. Bathymetry with mid-ocean ridges used  
 638 in series #1 and #2 (a), and flat-bottomed bathymetric reconstructions used in simulations  
 639 with no mid-ocean ridges (b) (see Extended Data Fig. 6). Only reconstructions for 0 to 140  
 640 Ma (both included) differ (see Methods). Emerged continental masses are shaded white.  
 641 Eckert IV projection.



642

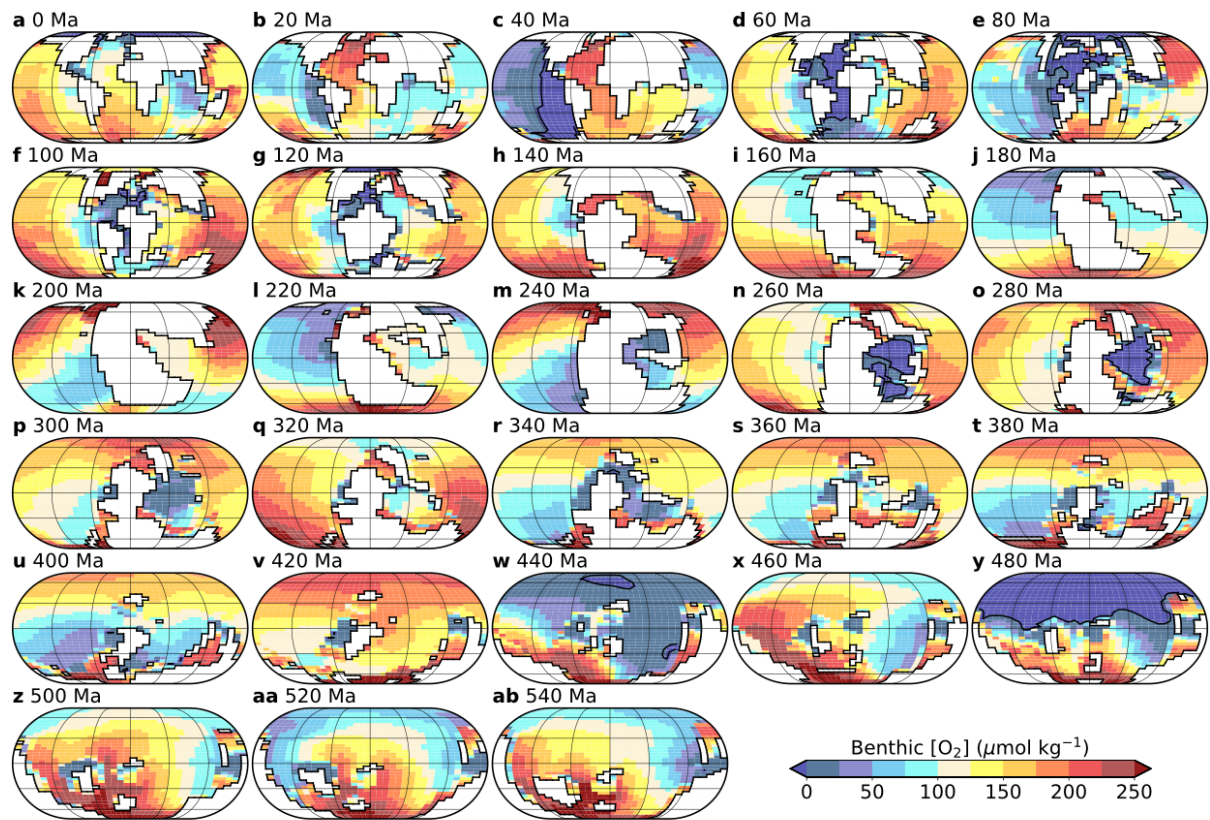
643 Extended Data Figure 8. Time-evolution of benthic  $[O_2]$ . (a) Simulations at 2240 ppm  $CO_2$

644 with temperature-dependent remineralization (series #1). (b) Simulations in which we varied

645  $p\text{CO}_2$  in order to approximately 'correct' for the paleogeographical impacts on climate (series

646 #2).

647

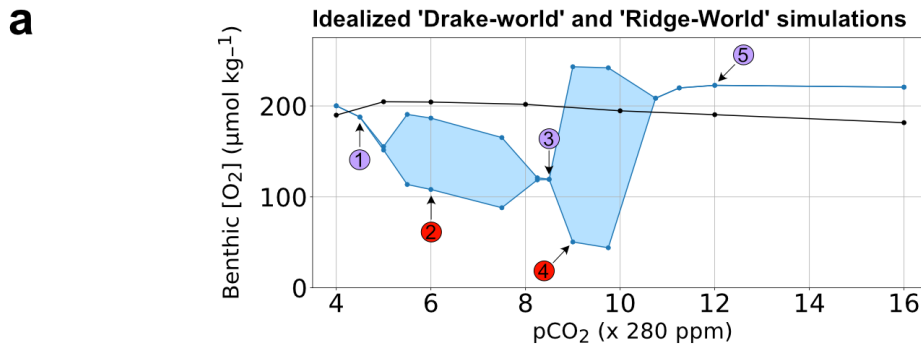


648

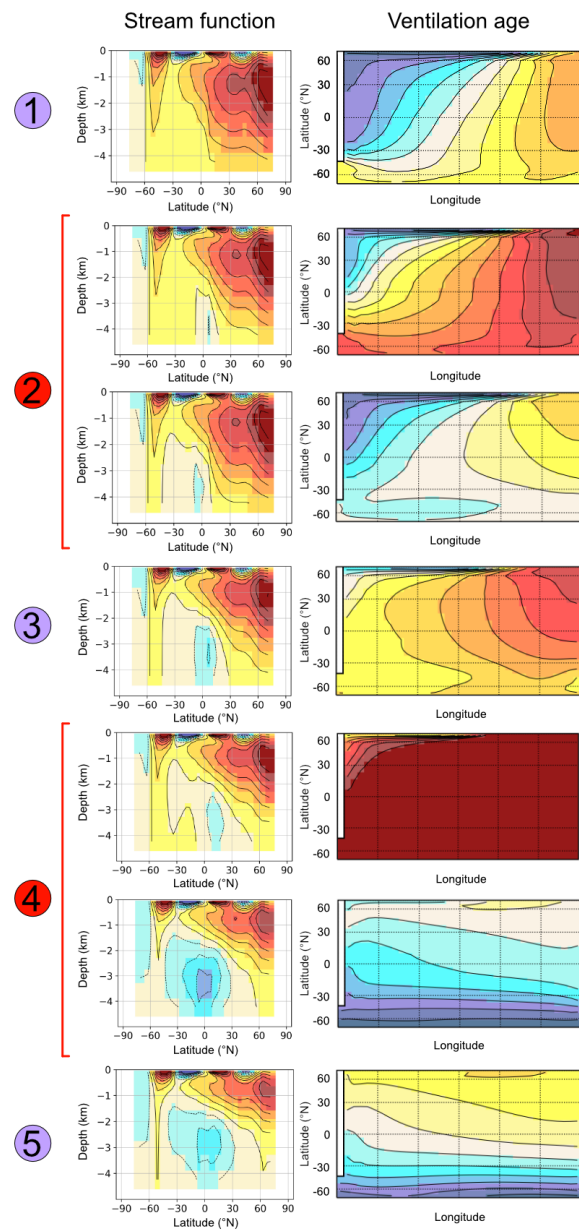
649 Extended Data Figure 9. Sensitivity of benthic [O<sub>2</sub>] to atmospheric forcing (pCO<sub>2</sub>). Benthic  
 650 oxygen concentrations for simulations at 1120 ppm CO<sub>2</sub>, with temperature-dependent  
 651 remineralization and mid-ocean ridges. Emerged continental masses are shaded white.  
 652 Results are averaged over the last 5000 years. Eckert IV projection.

653

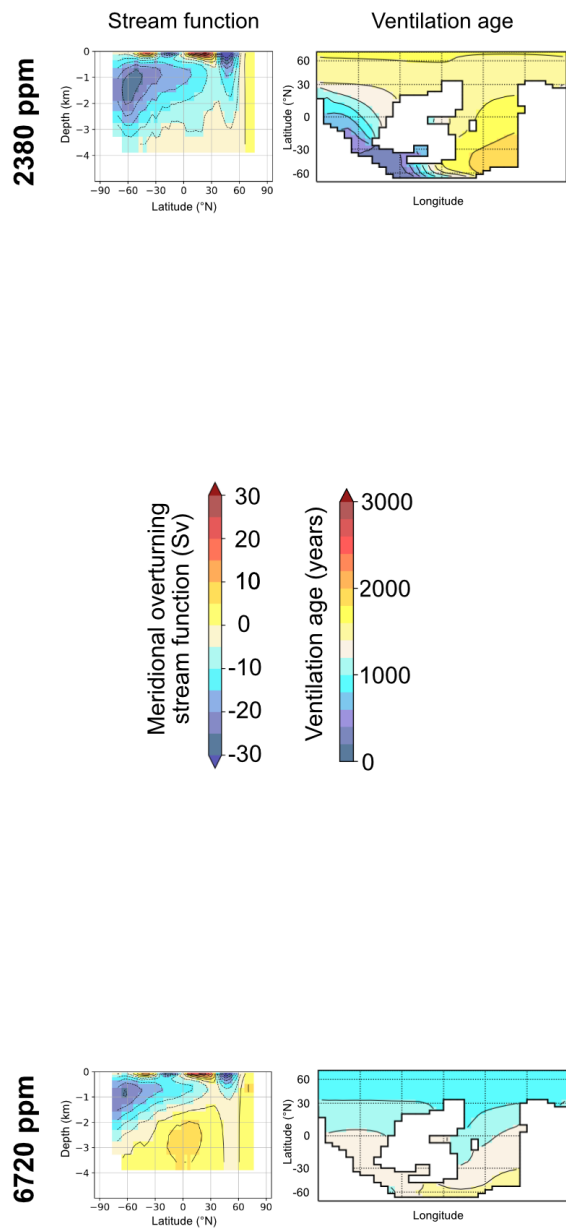
654



**b** Idealized 'Drake-world' simulations



**c** 'Realistic' latest Ordovician simulations



655

656 Extended Data Figure 10: Ocean circulation regimes in the cGENIE model. (a) Envelope of

657 benthic [O<sub>2</sub>] values simulated at various atmospheric CO<sub>2</sub> levels using Drake world (in blue,

658 see maps in panel (b)) and ridge world (in black) (Methods). Regimes of stable equilibria and  
659 regimes of stable oscillations for Drake World simulations are numbered and labelled using a  
660 blue and red background, respectively. (b) Meridional overturning stream function in Sv  
661 (sverdrup,  $1 \text{ Sv} = 10^6 \text{ m}^3 \text{ s}^{-1}$ ) and map of benthic ventilation age for each stable equilibrium  
662 and the 2 extreme states of each stable oscillatory regime identified in panel (a), using same  
663 numbering and color code. Lambert cylindrical equal-area projection. A negative (blue) stream  
664 function corresponds to an anticlockwise circulation. (c) Tentative comparison with the latest  
665 Ordovician simulations of Pohl et al.<sup>21</sup>. Results are shown at 6720 ppm and 2380 ppm CO<sub>2</sub>,  
666 corresponding to the warm and cold states of Scenario #1 in ref.<sup>21</sup>.